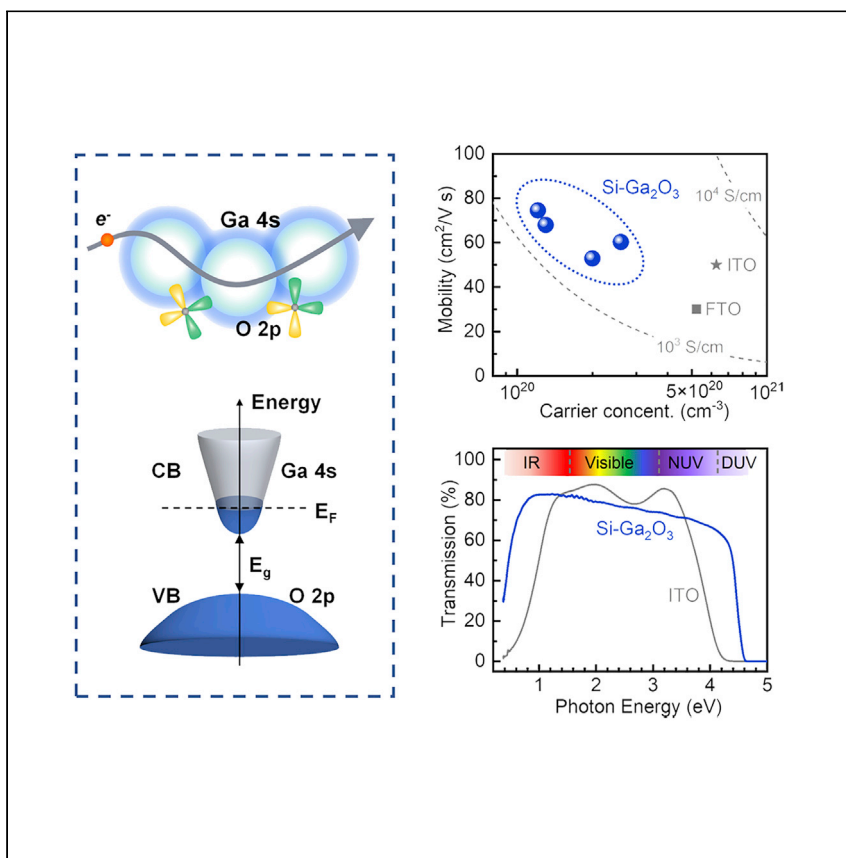


Article

# Deep UV transparent conductive oxide thin films realized through degenerately doped wide-bandgap gallium oxide



Zhang et al. report the achievement of a deep UV transparent, highly conductive, and low work-function thin film based on Si-doped  $\text{Ga}_2\text{O}_3$ . This work may provide significant guidance for the use of Si-doped  $\text{Ga}_2\text{O}_3$  thin films as electrodes in high-power electronics, deep UV, and organic electronic devices.

Jiaye Zhang, Joe Willis, Zhenni Yang, ..., Lang Chen, David O. Scanlon, Kelvin H.L. Zhang

chenlang@sustech.edu.cn (L.C.)  
d.scanlon@ucl.ac.uk (D.O.S.)  
kelvinzhang@xmu.edu.cn (K.H.L.Z.)

## Highlights

A deep UV transparent and highly conductive thin film based on SGO

Determination of the electronic structure of  $\text{Ga}_2\text{O}_3$  by experiments and calculations

Spatially extended Ga 4s orbitals are the key to the SGO's high conductivity



Article

# Deep UV transparent conductive oxide thin films realized through degenerately doped wide-bandgap gallium oxide

Jiaye Zhang,<sup>1,2</sup> Joe Willis,<sup>3,4,5</sup> Zhenni Yang,<sup>1</sup> Xu Lian,<sup>6</sup> Wei Chen,<sup>6</sup> Lai-Sen Wang,<sup>7</sup> Xiangyu Xu,<sup>1</sup> Tien-Lin Lee,<sup>5</sup> Lang Chen,<sup>2,\*</sup> David O. Scanlon,<sup>3,4,\*</sup> and Kelvin H.L. Zhang<sup>1,8,\*</sup>

## SUMMARY

Deep UV transparent thin films have recently attracted considerable attention owing to their potential in UV and organic-based optoelectronics. Here, we report the achievement of a deep UV transparent and highly conductive thin film based on Si-doped  $\text{Ga}_2\text{O}_3$  (SGO) with high conductivity of 2500 S/cm. The SGO thin films exhibit high transparency over a wide spectrum ranging from visible light to deep UV wavelength and, meanwhile, have a very low work-function of approximately 3.2 eV. A combination of photoemission spectroscopy and theoretical studies reveals that the delocalized conduction band derived from Ga 4s orbitals is responsible for the  $\text{Ga}_2\text{O}_3$  films' high conductivity. Furthermore, Si is shown to act as an efficient shallow donor, yielding high mobility up to approximately 60 cm<sup>2</sup>/Vs. The superior optoelectronic properties of SGO films make it a promising material for use as electrodes in high-power electronics and deep UV and organic-based optoelectronic devices.

## INTRODUCTION

Transparent conducting oxides (TCOs) constitute a unique class of materials that simultaneously possess seemingly conflicting properties of optical transparency and high electrical conductivity. TCOs have widespread applications as transparent electrodes in modern optoelectronics, including flat panel displays, solar cells and light-emitting diodes (LED).<sup>1,2</sup> At present, commercially used TCOs are based on degenerately doped wide-bandgap oxide semiconductors such as Sn doped  $\text{In}_2\text{O}_3$  (ITO), F-doped  $\text{SnO}_2$  (FTO), and Al-doped  $\text{ZnO}$  (AZO), in which a bandgap ( $E_g$ ) of greater than 3.2 eV maintains optical transparency for visible light, and degenerate doping provides an excellent electrical conductivity higher than 10<sup>3</sup> S/cm.<sup>3,4</sup>

However, with the rapid development of UV and organic-based optoelectronics in recent years, there is an increasing demand for new TCO materials with deep UV (deep UV, 200–300 nm in wavelength) transparency as efficient electrodes for deep UV lasers, deep UV LEDs and deep UV detectors. Deep UV LEDs and lasers are attracting considerable attention for various applications, including coronavirus sterilization, water purification, lithography, and biological detection,<sup>5</sup> but the efficiency of such a deep UV LED is quite low (only approximately 1%), in part because of the non-availability of a deep UV transparent electrode.<sup>6,7</sup> Conventional TCOs such as ITO, FTO and AZO are opaque in the deep UV region because of their small  $E_g$  of less than 3.5 eV.<sup>8</sup> Moreover, a TCO layer with a low work-function of 2.5–3.5 eV

<sup>1</sup>State Key Laboratory of Physical Chemistry of Solid Surfaces, College of Chemistry and Chemical Engineering, Xiamen University, Xiamen 361005, P.R. China

<sup>2</sup>Department of Physics, Southern University of Science and Technology, Shenzhen, Guangdong 518055, China

<sup>3</sup>Department of Chemistry, University College London, 20 Gordon Street, London WC1H 0AJ, UK

<sup>4</sup>Thomas Young Centre, University College London, Gower Street, London WC1E 6BT, UK

<sup>5</sup>Diamond Light Source Ltd., Harwell Science and Innovation Campus, Didcot OX11 0DE, UK

<sup>6</sup>Department of Chemistry, National University of Singapore, Singapore 117543, Singapore

<sup>7</sup>Fujian Key Laboratory of Materials Genome, College of Materials, Xiamen University, Xiamen 361005, P.R. China

<sup>8</sup>Lead contact

\*Correspondence:  
[chenlang@sustech.edu.cn](mailto:chenlang@sustech.edu.cn) (L.C.),  
[d.scanlon@ucl.ac.uk](mailto:d.scanlon@ucl.ac.uk) (D.O.S.),  
[kelvinzhang@xmu.edu.cn](mailto:kelvinzhang@xmu.edu.cn) (K.H.L.Z.)

<https://doi.org/10.1016/j.xcpr.2022.100801>



is also highly needed to increase the electron ejection efficiency into the given organic semiconductor in organic LED and organic thin-film transistors (OTFT),<sup>9–11</sup> as the work-functions of most TCOs are larger than 4.2 eV.<sup>11,12</sup>

Gallium oxide ( $\text{Ga}_2\text{O}_3$ ) is a semiconductor with an ultra-wide bandgap of 4.8 eV; therefore, it is transparent in the deep UV spectrum. The bandgap of  $\text{Ga}_2\text{O}_3$  is larger than other reported deep UV TCO materials, such as electron-doped  $12\text{CaO}\cdot7\text{Al}_2\text{O}_3$  ( $E_g \sim 4$  eV,  $\sigma \sim 800$  S cm $^{-1}$ ),<sup>13,14</sup>  $\text{Mg}_{0.43}\text{Zn}_{0.57}\text{O}$  ( $E_g \sim 4.2$  eV,  $\sigma \sim 400$  S cm $^{-1}$ ),<sup>15</sup> and  $\text{SrSnO}_3$  ( $E_g \sim 4.6$  eV, 3000 S cm $^{-1}$ ).<sup>16</sup> Recently,  $\text{Ga}_2\text{O}_3$  has been attracting considerable attention for application in high-power electronics and solar-blind UV (200–280 nm) photodetection, because of the ultra-wide bandgap, high theoretical breakdown field, and availability of large-scale wafers and stability.<sup>17–19</sup>  $\text{Ga}_2\text{O}_3$  is also amenable to degenerate *n*-type doping using group IV elements such as Si,<sup>20–22</sup> Ge,<sup>23</sup> and Sn,<sup>23</sup> rendering  $\text{Ga}_2\text{O}_3$  a promising candidate to be explored as a deep UV TCO. The technological importance of highly conductive  $\text{Ga}_2\text{O}_3$  has prompted a number of studies of electron doping of  $\text{Ga}_2\text{O}_3$ . Sn doped  $\text{Ga}_2\text{O}_3$  thin films were explored as a deep UV TCO 20 years ago,<sup>24</sup> but the conductivity was limited to a low value of approximately 1 S/cm. Recently, Leedy et al.<sup>22</sup> reported the achievement of a high conductivity of 732 S/cm based on Si-doped  $\text{Ga}_2\text{O}_3$  thin films. Heavily Si-doped  $\text{Ga}_2\text{O}_3$  layers with carrier concentration of  $5 \times 10^{19}$  cm $^{-3}$  have been used as low-resistance Ohmic contacts to a  $\text{Ga}_2\text{O}_3$  channel layer,<sup>25</sup> effectively reducing the parasitic resistance in  $\text{Ga}_2\text{O}_3$  modulation-doped high electron mobility transistors. However, thus far, the electrical conductivity of n-type doped  $\text{Ga}_2\text{O}_3$  achieved is still orders of magnitude lower than the minimum value of approximately 10 $^3$  S/cm required for TCOs. The fundamental optoelectronic properties and the potential of degenerately doped  $\text{Ga}_2\text{O}_3$  thin films as deep UV TCOs have not been fully explored yet.

In this work, we report the achievement of highly conductive and deep UV transparent oxide thin films based on Si-doped  $\text{Ga}_2\text{O}_3$  (SGO) with a record-high conductivity of 2,500 S/cm and mobility of 60 cm $^2$ /V s. The SGO thin films possess a high transparency of more than 80% in the wide spectrum from infrared to deep UV light wavelengths, and a work-function of as low as 3.2 eV, making it a promising UV transparent electrode for deep UV optoelectronics. A combination of hard X-ray photoemission spectroscopy (HAXPES), optical spectroscopy and density functional theory (DFT) calculations were also performed to reveal the fundamental insights into the electronic structures for the superior properties and reveal that the chemistry of the spatially extended Ga 4s-derived conduction band and effective Si doping are the key for high mobility and conductivity of SGO films.

## RESULTS AND DISCUSSION

### Thin-film growth and crystal structures

The most stable phase of  $\text{Ga}_2\text{O}_3$  is the monoclinic  $\beta$ -phase (hereafter referred to as  $\text{Ga}_2\text{O}_3$ ).<sup>26</sup> Figure 1A shows the crystal structure of  $\text{Ga}_2\text{O}_3$  (left), consisting of tetrahedrally ( $T_d$ ) coordinated  $\text{Ga}_1$  and octahedrally ( $O_h$ ) coordinated  $\text{Ga}_2$  sites. The conduction band (CB) of  $\text{Ga}_2\text{O}_3$  (right, Figure 1A) is mainly derived from the spatially extended Ga 4s orbital, giving rise to a dispersive CB edge and high mobility for conduction of electrons.<sup>27</sup> Si doping in  $\text{Ga}_2\text{O}_3$  preferentially substitutes for Ga at the  $\text{Ga}_1$  site,<sup>28,29</sup> effectively adding extra electrons to the bottom of CB. We grew approximately 200-nm-thick SGO thin films with Si doping levels of  $x = 0.01\%$ ,  $0.03\%$ ,  $0.1\%$ ,  $0.5\%$ ,  $1\%$ , and  $2\%$  on (010)-oriented  $\text{Ga}_2\text{O}_3$  substrates using pulsed laser deposition. Details for thin film growth and characterizations are provided in

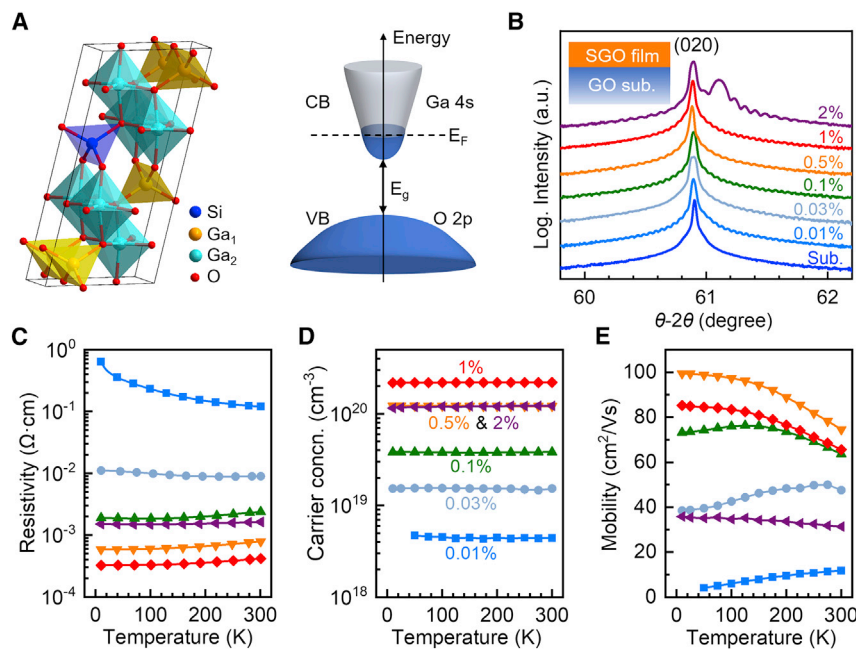


**Figure 1. Crystal structure and temperature-dependent transport properties**

(A) Left: Crystal structure of monoclinic  $\text{Ga}_2\text{O}_3$  doped with Si at the  $T_d$ -coordinated Ga site; Ga cations located at  $T_d$  ( $\text{Ga}_1$ , yellow) and  $O_h$  ( $\text{Ga}_2$ , cyan) coordination. Right: Schematic energy diagram for  $\text{Ga}_2\text{O}_3$ , showing the Ga 4s derived CB and O 2p derived VB.

(B) Out-of-plane  $\theta$ -2 $\theta$  XRD patterns in the vicinity of  $\text{Ga}_2\text{O}_3$  (020) reflections. Pronounced Kiessig interference fringes confirm the high crystalline quality of the epitaxial films.

(C–E) Temperature dependence of (C) resistivity, (D) carrier concentration, and (E) hall mobility for  $(\text{Si}_x\text{Ga}_{1-x})_2\text{O}_3$  with different  $x$ .

the [experimental procedures](#) section. [Figure 1B](#) show  $\theta$ -2 $\theta$  X-ray diffractometer (XRD) patterns around the (020) diffraction peak of  $\text{Ga}_2\text{O}_3$ . For  $x \leq 1\%$ , the film (020) peaks overlap with that of the substrate, suggesting that the films have very similar lattice constants as bulk  $\text{Ga}_2\text{O}_3$  (3.037 Å). However, for the  $x = 2\%$  films, the out-of-plane lattice constants are slightly smaller than that bulk  $\text{Ga}_2\text{O}_3$  substrate. The shrinkage of the lattice constant is due to the smaller ionic radius of  $\text{Si}^{4+}$  (0.54 Å) than  $\text{Ga}^{3+}$  (0.76 Å) at the  $T_d$   $\text{Ga}_1$  coordinated site, indicating the successful incorporation of Si at the Ga lattice site. Furthermore, all the films exhibit well-defined Kiesig fringes and have similar full-width-at-half-maximum as the substrate in the XRD rocking curve ([Figure S1](#)), confirming the high crystalline quality of the films. atomic force microscopy images ([Figure S2](#)) also shows the films have smooth surfaces with a root-mean-square roughness of less than 0.6 nm.

### Transport and optical properties

Temperature-dependent transport properties were measured from 10 to 300 K. The corresponding electrical resistivity ( $\rho$ ), carrier concentration ( $n_e$ ), and mobility ( $\mu$ ) are shown in [Figures 1C–1E](#). The 0.01% SGO film with  $n_e = 5.6 \times 10^{18} \text{ cm}^{-3}$  exhibits semiconducting behavior, whereas films with higher doping levels show clear characteristics of metallic conductivity, indicating the degenerate doping of  $\text{Ga}_2\text{O}_3$ . Using the reported static dielectric constant  $\epsilon_s$  of 10.2 and electron effective mass  $m_0^*$  of 0.28  $m_e$ ,<sup>30,31</sup> the effective Bohr radius  $a_B^* = a_H \epsilon_s / (m_0^* / m_e)$  for a donor state in  $\text{Ga}_2\text{O}_3$  is estimated to be 1.9 nm. The critical carrier concentration  $n_c$  for the onset of degenerate metallic conductivity as defined by the Mott criterion  $(n_c)^{1/3} a_B^* \approx 0.25$  is calculated to be approximately  $3 \times 10^{18} \text{ cm}^{-3}$ .<sup>32</sup> The overall trend of

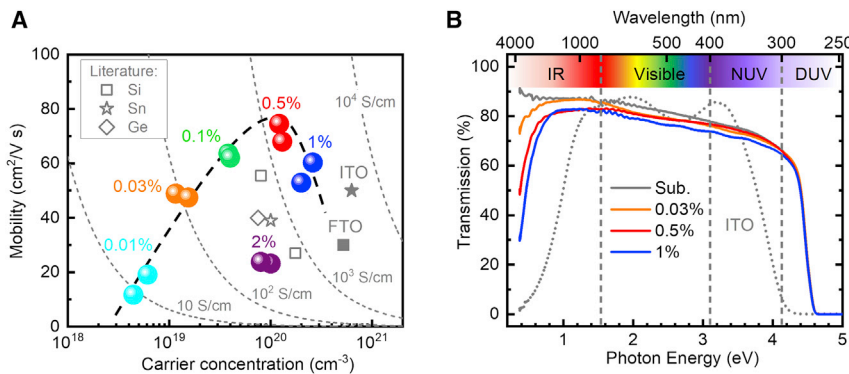


**Figure 2. Room temperature transport and optical properties**

(A) Room temperature Hall mobility as a function of carrier concentration for the SGO thin films deposited by pulsed laser deposition in this work, and Si, Sn, and Ge doped thin films reported in the literature<sup>23,33,34</sup> as well as ITO and FTO.<sup>1,2</sup> The gray dashed lines display the lines of constant conductivity.

(B) The wide-range optical transmission of  $\text{Ga}_2\text{O}_3$  substrate (Sub.) and approximately 200 nm-thickness 0.03%, 0.5 and 1% Si doped  $\text{Ga}_2\text{O}_3$  thin films (on  $\text{Ga}_2\text{O}_3$  substrate), as well as approximately 200 nm-thickness ITO on  $\text{SiO}_2$  substrate. DUV, deep UC; IR, infrared; NUV, near UV.

transport properties of our films with different doping levels agrees fairly well with the prediction based on the Mott criterion for metal-insulator transitions. Figure 2A and Table 1 summarize the room temperature  $n_e$ ,  $\mu$ , and electrical conductivity ( $\sigma$ ) of our films, alongside other n-type doped  $\text{Ga}_2\text{O}_3$  films reported in the literature,<sup>23,33,34</sup> as well as ITO and FTO.<sup>1,2</sup> It can be seen that the 0.5% and 1% doped SGO films possess very high  $\mu$  values up to  $75 \text{ cm}^2/\text{Vs}$  and  $65 \text{ cm}^2/\text{Vs}$  respectively, and high  $n_e$  of more than  $10^{20} \text{ cm}^{-3}$ , indicating the superior electrical properties of the SGO films. We found the electrical properties of SGO is very sensitive to the growth temperature and oxygen pressure. With an optimized growth temperature of  $600^\circ\text{C}$  and oxygen pressure of  $10 \text{ mTorr}$ , we have achieved a record highest  $\sigma$  of  $2500 \text{ S/cm}$  and  $n_e$  of up to  $2.6 \times 10^{20} \text{ cm}^{-3}$  for the 1% Si-doped films. The  $\sigma$  and  $n_e$  of the 0.5 and 1% SGO are competitive with those of conventional ITO and FTO thin films and can meet the requirements for optoelectronic device applications.<sup>1</sup> We also found that the crystalline quality has a considerable effect on the mobility of thin films. Under the same growth conditions, the hetero-epitaxial thin films grown on  $\text{Al}_2\text{O}_3$  substrates normally exhibit a low mobility of  $2 \text{ cm}^2/\text{V s}$ . This is likely due to the scattering from the defects and/or grain boundaries in the hetero-epitaxial films.<sup>35,36</sup>

Figure 2B shows the optical transmittance for the SGO films together with the  $\text{Ga}_2\text{O}_3$  substrates. Despite its large thickness of approximately 0.5 mm, the  $\text{Ga}_2\text{O}_3$  substrate still shows a high average transmittance greater than 80% in the visible range (400–700 nm in wavelength). Moreover, the  $\text{Ga}_2\text{O}_3$  substrate also exhibits a high transparency in the deep UV region, e.g., 65% at 300 nm. The SGO films grown on  $\text{Ga}_2\text{O}_3$  substrates show quite similar transparency from visible light to deep UV spectrum, as summarized in Table 1, but the transparent window of the SGO films is re-set at the infrared region by plasmon energy arising from doped free electrons, and extended to shorter UV wavelengths owing to the widening of the optical bandgap. The plasmon energy ( $w_p$ ) is proportional to  $n_e^{1/2}$  by  $w_p^2 = n_e e^2 / m * \epsilon_\infty \epsilon_0$ . The plasmon energies derived from carrier concentrations are summarized in Table 1. At UV wavelengths, the cutoff is slightly extended to shorter UV wavelengths owing to the increase of optical bandgap from 4.80 eV to 4.99 eV arising from the filling of the lower

**Table 1. The summary of electrical and optical properties for Si doped Ga<sub>2</sub>O<sub>3</sub>**

x	$\sigma$ (S/cm)	$n_e$ (cm <sup>-3</sup> )	$\mu$ (cm <sup>2</sup> /V s)	T <sub>vis</sub> (%)	T <sub>UV</sub> (%)	E <sub>VBM</sub> (eV)	$\omega_p$ (eV)	$\Phi_w$ (eV)
0.01%	18.6	$5.6 \times 10^{18}$	20.7	NA	NA	4.80	0.067	3.26
0.03%	111	$1.5 \times 10^{19}$	47.5	80.3	67.2	4.85	0.144	3.34
0.1%	378	$3.8 \times 10^{19}$	62.1	NA	NA	4.89	0.175	3.39
0.5%	1,322	$1.1 \times 10^{20}$	75.0	80.1	67.4	4.97	0.297	3.43
1%	2,500	$2.6 \times 10^{20}$	60.3	78.6	65.1	4.99	0.456	3.45

Room temperature conductivities ( $\sigma$ ), carrier concentration ( $n_e$ ), mobility ( $\mu$ ), averaged transmission in the visible (T<sub>vis</sub>, at wavelengths of 420, 490, 560, 630 and 700 nm), and UV region (T<sub>UV</sub>, at wavelengths of 280, 310, 340, 370, and 400 nm), HAXPES measured VBM (E<sub>VBM</sub>), plasmon energy ( $\omega_p$ ) derived from carrier concentration, and work-function ( $\Phi_w$ ) for SGO thin films on a Ga<sub>2</sub>O<sub>3</sub>(010) substrate.

CB states by degenerately doped electrons, i.e., the Burstein-Moss shift.<sup>37,38</sup> We will discuss the determination of the change of the optical bandgaps using HAXPES in the following section.

To clearly compare the optical transmission and conductivity of SGO with other reported deep UV TCO materials, we introduce Haacke's figure-of-merit  $\varphi_{TC} = T^{10}/R_s$ ,<sup>39</sup> where  $T$  is the transmission and  $R_s$  is the sheet resistance. The  $\varphi_{TC}$  of the present SGO film is  $3.8 \times 10^{-4} \Omega^{-1}$ , which is much higher than that of other reported deep UV TCO materials, such as electron-doped 12CaO·7Al<sub>2</sub>O<sub>3</sub> ( $10^{-7} \Omega^{-1}$ )<sup>13,14</sup> and Mg<sub>0.43</sub>Zn<sub>0.57</sub>O ( $10^{-12} \Omega^{-1}$ )<sup>15</sup> and is compared with that of recently reported La-doped SrSnO<sub>3</sub> ( $8.6 \times 10^{-4} \Omega^{-1}$ )<sup>16</sup> at 300 nm in wavelength. The high electrical conductivity and outstanding transparency up to the deep UV spectrum of the SGO films make them promising materials as efficient electrode layers for deep UV LED and lasers, as well as low-resistance Ohmic contacts in high-power electronics. For example, recently deep UV LEDs are attracting considerable attention for various applications including coronavirus sterilization, lithography, and biological detection.<sup>5</sup> However, the current external quantum efficiency of such a deep UV LED is quite low (only around 1%), in part because of the non-availability of a deep UV transparent electrode.<sup>6,7</sup> The SGO films can meet the requirement for conductivity and deep UV transparency. Unlike conventional TCO thin films, which are typically grown on glass or Al<sub>2</sub>O<sub>3</sub> substrates,<sup>40,41</sup> the present high conductive and UV transparent SGO thin films are homoepitaxially grown on Ga<sub>2</sub>O<sub>3</sub> substrates. Nevertheless, the present SGO thin films have a promising potential for many optoelectronic device applications. First, a large size Ga<sub>2</sub>O<sub>3</sub> substrate with a high transmittance of more than 80% in the spectrum from infrared to deep UV range, are commercially available and its price is expected to gradually decrease.<sup>42</sup> Second, at present, most of the Ga<sub>2</sub>O<sub>3</sub>-based power electronics devices, e.g., field-effect transistors, are homoepitaxially grown on Ga<sub>2</sub>O<sub>3</sub> substrate. The homo-epitaxially grown SGO layers with high conductivity are much needed to be used as low-resistance ohmic contacts to a Ga<sub>2</sub>O<sub>3</sub> channel layer.<sup>25</sup>

### Electronic structure

To gain deep insights on the optical and electronic properties, HAXPES measurements at the CB and valence band (VB) as well as hybrid DFT calculations were performed. Based on hybrid DFT density of state calculations, the VB of Ga<sub>2</sub>O<sub>3</sub> is mainly derived from the filled O 2p<sup>6</sup> orbital, and the CB primarily from the Ga 4s orbital. The spatially extended Ga 4s orbital leads to highly dispersive CB edges and thus small effective masses for high electron mobility. HAXPES enhances the ability to detect Ga 4s orbital owing to the enhanced photoionization cross-section for Ga 4s orbital relative to O 2p at higher excitation photon energies.<sup>43</sup> This makes it a very effective way to directly observe the electronic states of the filled electrons at

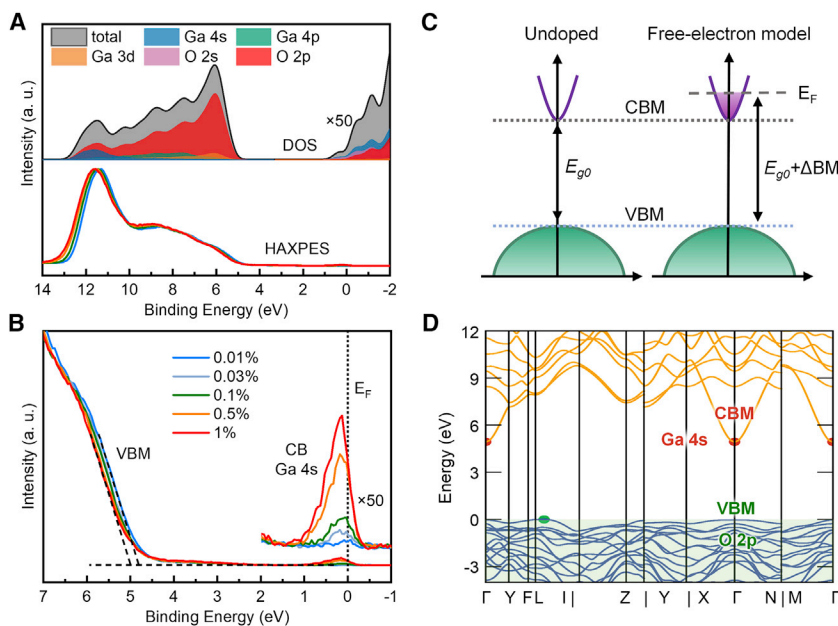


**Figure 3. Electronic structure of Ga<sub>2</sub>O<sub>3</sub>**

- (A) The calculated partial and total density of state (top) for undoped Ga<sub>2</sub>O<sub>3</sub>, as well as the experimental HAXPES spectra (bottom) plotted as a function of binding energy.
- (B) The expanded view of VB edge ( $\times 3$ ) and CB ( $\times 50$ ) for the (Si<sub>x</sub>Ga<sub>1-x</sub>)<sub>2</sub>O<sub>3</sub> with different x.
- (C) Schematic diagram of the change in electronic structure for undoped and degenerately doped Ga<sub>2</sub>O<sub>3</sub>. Doping produces an increase of optical bandgap ( $E_{\text{opt}}$ ), consisting the contributions from Burstein-Moss shift ( $\Delta BM$ ).
- (D) HSE06 calculated band structures for undoped Ga<sub>2</sub>O<sub>3</sub>.

the Ga 4s-derived CB. Figures 3A and 3B show the HAXPES spectra, encompassing the VB, CB, and the bandgap region. Based on a free-electron model, using the  $n_e$  determined from transport measurement, the 0.01% SGO is close to the threshold of degenerate doping and its  $E_F$  is just 0.02 eV above the CB minimum (CBM). A well-defined CB feature straddling the Fermi level ( $E_F$ ) is observed for a higher Si doping level (Figure 3B inset), resulting from the filled electrons at the bottom of CB. As expected, the intensity of the occupied CB feature progressively increases with the Si doping level. The electrons occupying the highly dispersive CB leads to free electron-like metallic properties, consistent with the temperature-dependent transport measurement.

Turn to the VB spectra. Concurrently with the filling of CB by electrons, the VB maximum (VBM) also shifts to higher binding energy, owing to the upshift of the  $E_F$ , as shown in Figure 3B and Table 1. The VBM for 0.01% SGO is determined to be at 4.80 eV below the  $E_F$ . This value is approximated as the bandgap of Ga<sub>2</sub>O<sub>3</sub>, since the  $E_F$  of the 0.01% SGO is close to the CBM. With increasing Si, the optical bandgap of SGO increases because of the block of the lower CB states by filled electrons, i.e., Burstein-Moss shift. Based on a free electron model, the  $E_F$  for 0.5 and 1% SGO are estimated to be at 0.34 and 0.51 eV above the CBM (see Figure 3C), i.e., the optical bandgap should be increased by 0.34 and 0.51 eV, respectively. However, the increase of bandgap is further counteracted by bandgap shrinkage owing to many-body interactions arising from electron-electron interaction and electron-ion interaction in degenerate doping levels.<sup>44</sup> Nonetheless, as illustrated in Figures 3B and 3C, because HAXPES measures both the CB and VB features with the  $E_F$  referred to as zero energy, the measured energetic separation between the VBM

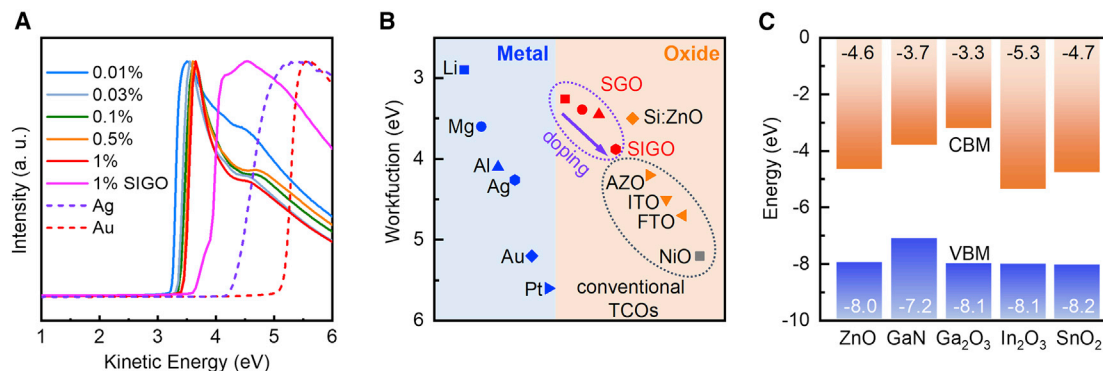


**Figure 4. Work function and band structure**

(A) Secondary energy cutoff used to measure the work-function of the SGO thin films and Ag, Au foils.

(B and C) (B) The workfunction values of various metals and TCOs.<sup>11,12</sup> (C) Valence and CB with respect to the VL for ZnO, GaN, ITO, and SnO<sub>2</sub> taken from the recent calculations,<sup>46–48</sup> as well as that of Ga<sub>2</sub>O<sub>3</sub> from our experiment. The VL is set to 0 eV. The EA and ionization potential values are indicated at the top and bottom of the figure, respectively.

and E<sub>F</sub> (E<sub>F</sub>-VBM) in HAXPES reflects the onset of optical absorption or E<sub>opt</sub>. Therefore, we take the E<sub>F</sub>-VBM values as optical bandgaps of SGO. It can be seen that Si doping widens the transparent window at deep UV spectrum by increasing the optical bandgaps, up to 4.99 eV for 1% SGO. Based on the HAXPES results and DFT calculations, it can be concluded that the high density of free electrons filled at the highly dispersive Ga 4s-derived CB is responsible for the highly conductive SGO thin films, notably with 0.5 and 1% Si doping levels. Figure 3D shows the DFT calculated band structure of Ga<sub>2</sub>O<sub>3</sub>. The CB edge of Ga<sub>2</sub>O<sub>3</sub> consists of a highly dispersive Ga 4s derived band, leading to a low effective electron mass of 0.28 m<sub>e</sub>\* and large orbital overlapping for high electron mobility. DFT calculations also indicate the 3s dopant state of Si are energetically separated from the Ga 4s-derived CBM, and can easily donate the extra electrons to the delocalized CB of Ga<sub>2</sub>O<sub>3</sub>. Furthermore, because there is no hybridization of Si donor orbitals with the Ga 4s CBM states, the low effective mass of Ga<sub>2</sub>O<sub>3</sub> is retained even with a high Si doping level, therefore leading to the high electron mobility in the degenerately SGO.

#### Band structure and work-function

We measured the work-function of the SGO films using UV photoemission spectroscopy, as shown in Figure 4A. It is interesting to note that SGO has lower work-function values of 3.26–3.45 eV. Notably, the work-function of SGO films are much lower than those of conventional TCOs, such as ITO (approximately 4.5 eV), FTO (approximately 4.7 eV), and AZO (approximately 4.2 eV),<sup>11,12</sup> as shown in Figure 4B. Oxide semiconductors rarely have work-functions that are lower than 4 eV. The low work-functions of SGO films has significant implications for their use as efficient electron injection layers in organic LED and OTFT, which require efficient band alignment between the low work-functions of the cathode organic semiconductors. Most of the organic semiconductors in organic LED and OTFT have a rather small electron affinity (EA) of less than 3.5 eV.<sup>9–11,45</sup> A low work-function and stable electrode material are highly needed to minimize the interfacial energy barriers for electron injection into the lowest unoccupied molecular orbital of organic semiconductors to maximize device efficiency. However, at present, the lack of stable low work-function electrode materials still limits the device efficiency.<sup>11,12</sup>

Moreover, it is also of interest to discuss the low work-function of SGO in comparison with conventional TCOs such as ITO, FTO, and AZO, in terms of the electronic

structure. Figure 4C summarizes the energy positions of CB and VB edges of ZnO, GaN, ITO, and SnO<sub>2</sub> relative to the vacuum level (VL) taken from the recent calculations,<sup>46–48</sup> as well as that of Ga<sub>2</sub>O<sub>3</sub> from our experiment. The CB edges for all these wide bandgap semiconductors are formed by the empty ns orbitals of metal cations. An important factor explaining the low work-function of SGO is the relatively high energy position of the Ga 4s derived CB,<sup>49</sup> which results in a very small EA value of 3.0 eV for Ga<sub>2</sub>O<sub>3</sub>. This, coupled with the high energy position of the E<sub>F</sub> lifted by degenerately doped electrons, results in the low work-function. A similar explanation also applies to GaN in which the Ga 4s-derived CB also results in a small EA value of 3.7 eV,<sup>46,48</sup> and degenerately n-type doped GaN has low work-function values of approximately 3.8 eV. In contrast, the low-lying Zn 4s in ZnO, Sn 5s in SnO<sub>2</sub>, and In 5s in ITO result in larger EAs and correspondingly larger work-functions.

In contrast, the high energy position of CB and small EA in Ga<sub>2</sub>O<sub>3</sub> also pose a hindrance to the n-type dopability of the free electron concentration, because the higher CB energy position limits its ability to accommodate doped electrons.<sup>48,50,51</sup> The highest n<sub>e</sub> in Ga<sub>2</sub>O<sub>3</sub> so far is  $2.6 \times 10^{20} \text{ cm}^{-3}$  achieved in the present work. In comparison, an n<sub>e</sub> of approximately  $10^{21} \text{ cm}^{-3}$  can be achieved in Sn doped ITO.<sup>1,2</sup> ITO has the lowest CB level of all the TCOs, which correlates with its ability to sustain the highest n<sub>e</sub> and highest σ (>10<sup>4</sup> S/cm<sup>2</sup>) when doped with 6% Sn. This is due to the relativistic contraction of the In 5s orbitals which causes the In 5s state to be located at lower energies relative to the VL.<sup>49</sup> This indicates that alloying Ga<sub>2</sub>O<sub>3</sub> with ITO could increase the n-type dopability of Ga<sub>2</sub>O<sub>3</sub>, and as such, increase the electrical conductivity. This type of rationale has been successfully used to increase the EA of ITO by alloying with Ti<sub>2</sub>O<sub>3</sub>.<sup>52</sup> Furthermore, the work-function of the films can also be tuned, because of the change of EAs. To verify this, we grew 1% Si-doped 90% Ga<sub>2</sub>O<sub>3</sub> alloyed with 10% ITO thin film, i.e., 1% Si-doped (In<sub>0.1</sub>Ga<sub>0.9</sub>)<sub>2</sub>O<sub>3</sub>, referenced as SIGO. The SIGO thin film has a high σ of 2100 S/cm and an n<sub>e</sub> of  $2.6 \times 10^{20} \text{ cm}^{-3}$ . As shown in Figures 4A and 4B, the SIGO film indeed has a work-function of 3.88 eV. The tuning of electronic properties and work-function by alloying with ITO would offer great potential to extend the applications of the current commercialized ITO if alloyed with Ga<sub>2</sub>O<sub>3</sub>, and vice versa for SGO if alloyed with ITO.

In summary, this work reported the achievement of deep UV transparent, highly conductive, and low work-function SGO thin films. The combined HAXPES and theoretical calculations clearly demonstrate their superior optoelectronic properties exhibit strong correlations with the chemistry of Ga 4s derived CB and doping effect of Si. The high conductivity of SGO is attributed to the high density of the free electrons induced by Si doping filled at the highly dispersive Ga 4s derived CB, while the low work-function of SGO is owing to high energy position of Ga 4s derived CB and thus small EA. Remarkably, with the introduction of a much lower In 5s orbital into the CB, its work-function can be tuned by alloying with ITO. The present results advance our fundamental understanding and provide important guidance for use of SGO and its alloying in UV and organic-based optoelectronics and high-power electronics.

## EXPERIMENTAL PROCEDURES

### Resource availability

#### Lead contact

Further information and requests for resources should be directed to and will be fulfilled by the lead contact, Prof. Kelvin. H. L. Zhang ([Kelvinzhang@xmu.edu.cn](mailto:Kelvinzhang@xmu.edu.cn)).

#### Materials availability

This study did not generate new material structures.

#### Data and code availability

This study did not produce new code. All of the data associated with this study can be found in the article or [supplemental information](#) and are available from the authors upon reasonable request.

#### Material synthesis

Ga<sub>2</sub>O<sub>3</sub> targets with Si doping concentrations of 0.01%, 0.03%, 0.1%, 0.5%, and 1% [i.e., Si/(Si + Ga)] were made by mixing and grinding the appropriate proportions of Ga<sub>2</sub>O<sub>3</sub> (99.999%, Alfa Aesar) and SiO<sub>2</sub> (99.999%, Alfa Aesar) polycrystalline powder, followed by cold pressing and sintering in air at 1,350°C for 24 h. SGO thin films were homoepitaxially grown on Fe-doped semi-insulating (010) β-Ga<sub>2</sub>O<sub>3</sub> substrates (Novel Crystal Technology) by pulsed laser deposition using a KrF excimer laser source ( $\lambda = 248$  nm,  $\tau = 25$  ns, Coherent COMPex 102) from respective targets. The doping level (x) are Si nominal values calculated from the mole ratio of Si to Ga in the targets. Before being loaded into the pulsed laser deposition chamber, the substrates were cleaned sequentially by acetone, isopropanol, and deionized water in the ultrasonic bath for 5 min and dried by nitrogen. During the growth, laser ablation was performed at a repetition rate of 5 Hz and an energy density of 1.2 J cm<sup>-2</sup>. Films were grown at a substrate temperature of 600°C in 10 mTorr O<sub>2</sub> with a target-substrate distance of 50 mm and cooled to room temperature in the same O<sub>2</sub> pressure. The target of 1% Si-doped (In<sub>0.1</sub>Ga<sub>0.9</sub>)<sub>2</sub>O<sub>3</sub> were made by a similar preparation method with the addition of appropriate proportions of ITO (99.999%, Alfa Aesar) polycrystalline powder and the corresponding films were prepared by the above growth method.

#### Crystal structure characterization

The crystal structures of thin films were determined by Rigaku SmartLab high-resolution XRD, using Cu K $\alpha$  radiation ( $\lambda = 0.15406$  nm) and parallel beam optics. High-resolution XRD 0-2θ scans and rocking curves were performed in standard symmetric geometry to examine the out-of-plane epitaxial relationship and crystalline quality. The thicknesses of thin films ranging from 180 to 220 nm were calculated from the positions of their Kiessig fringes. Film morphology was characterized using atomic force microscopy (Asylum Research MFP-3D-SA) at room temperature.<sup>53,54</sup> The experiments were carried out in the tapping mode with a scan speed of 10 μm/s, using Olympus standard silicon cantilevers (AC240TS-R3).

#### Optical and electrical measurements

Optical transmission spectra were collected at room temperature using a Cary 5000 spectrophotometer over the spectral range from 0.5 to 5.5 eV. The temperature-dependent electrical properties of the samples were characterized using a physical property measurement system (PPMS) in van der Pauw 4-point configuration. Ohmic contact pads with a metal stack of 5 nm Ni/100 nm Au were deposited by magnetron sputtering at the corners of the rectangular samples. The contact pads were bonded through aluminum wires to the channels of the PPMS dc resistivity puck.

#### Photoemission spectroscopy measurements

The HAXPES measurements were conducted at beamline I09 (Diamond Light Source, UK). The endstation is equipped with a VG Scienta EW4000 electron analyzer with ±30° angular acceptance. HAXPES samples were prepared by

mounting the thin films on copper sample holders with carbon tape and placing Cu foil in an electrical contact with contact pads (5 nm Ni/100 nm Au) on the films' surface to avoid charging effects. For core-level and VB scans, the pass energy and step size were set at 200 and 0.05 eV, resulting in an overall energy resolution of approximately 0.25 eV at a photon energy of 6,000 eV. The absolute binding energy scale was calibrated by an Au foil using Au's Fermi edge cutoff at  $0 \pm 0.02$  eV and 4f<sub>7/2</sub> core level at  $84.00 \pm 0.02$  eV. The probing depth was estimated to be approximately  $3\lambda$  of 24.2 nm, where  $\lambda = 8.1$  nm refers to VB electron's inelastic mean free path, as calculated by TPP-2M method in NIST's database.<sup>55</sup> UV photoemission spectroscopy measurements were carried out in a customer-designed ultrahigh vacuum system (base pressure  $\approx 10^{-10}$  mbar) with He I (21.22 eV) as the excitation source. The sample was held by a Ta foil, which also provided electrical contact with contact pads (5 nm Ni/100 nm Au) on the samples' surface to avoid charging effects. By applying a sample bias of -5 V, the work-function of the sample was determined by the secondary electron cut-off in the low kinetic energy region. SGO thin films were cleaned after transfer through air to the photoemission setup by annealing at 200°C in 100 mbar O<sub>2</sub> for 30 min.

### DFT calculations

DFT calculations were performed using the periodic code VASP (version 5.4.4),<sup>56–59</sup> which uses a plane-wave basis set and describes the interactions between valence and core electrons using the projector augmented wave (PAW) method.<sup>60,61</sup> Ga [3d<sup>10</sup>4s<sup>2</sup>4p<sup>1</sup>] and O[2s<sup>2</sup>2p<sup>4</sup>] PAW pseudopotentials were chosen for this work. The HSE06 hybrid exchange-correlation functional,<sup>62</sup> with an increased Hartree-Fock mixing parameter  $\alpha$  of 32%, was used to accurately reproduce the bulk bandgap and lattice parameters of Ga<sub>2</sub>O<sub>3</sub>, as has been performed in other computational studies of Ga<sub>2</sub>O<sub>3</sub> in the literature.<sup>28,63,64</sup> A plane-wave cut-off of 475 eV and bulk  $\Gamma$ -centered k-point mesh of  $8 \times 8 \times 4$  were found to converge the total energy to less than 1 meV per atom and accurately describe the electronic structure. An 80 atom supercell and relevant input files were generated using many of the tools available in the PyCDT package.<sup>65</sup> Analysis and plotting of band structures were performed with the sumo python package.<sup>66</sup>

### SUPPLEMENTAL INFORMATION

Supplemental information can be found online at <https://doi.org/10.1016/j.xrps.2022.100801>.

### ACKNOWLEDGMENTS

K.H.L.Z. is grateful for funding support from the National Natural Science Foundation of China (Grant No. 21872116 and 22075232). L.C. acknowledges support by the National Natural Science Foundation of China (No. 51972160) and the Science and Technology Research Items of Shenzhen (JCYJ20170412153325679, JCYJ20180504165650580). J.W. and D.O.S. acknowledge Diamond Light Source for co-sponsorship of an EngD studentship on the EPSRC Centre for Doctoral Training in Molecular Modeling and Materials Science (EP/L015862/1). D.O.S. acknowledges support for EPSRC (Grant number EP/N01572X/1). J.W. and D.O.S. acknowledge the use of the UCL Thomas High Performance Computing Facility (Thomas@UCL), and associated support services, in the completion of this work. W.C. acknowledges the support by the Singapore MOE (Grant MOE-000150-00). L.S.W. acknowledges the support of National Natural Science Foundation of China (Grant No. 51771157). We are grateful to the Diamond Light Source for access to beamline I09 under proposal number SI24219.

## AUTHOR CONTRIBUTIONS

J.Z. and K.H.L.Z. designed and conducted the experiments. J.Z. wrote the paper. J.W. and D.O.S. performed the theoretical calculations. J.W. and Z.Y. helped revise the paper. X.L. and W.C. performed the UV photoemission spectroscopy characterization. L.S.W. and X.X. performed the electrical characterization. T.-L. L. performed the HAXPES characterization. L.C., D.O.S., and K.H.L.Z. provided all support needed in this work. All authors contributed to the general discussion.

## DECLARATION OF INTERESTS

The authors declare they have no financial interests. D.O.S. is on the advisory board of *Cell Reports Physical Science* and receives no compensation as a member of the advisory board.

Received: December 1, 2021

Revised: January 24, 2022

Accepted: February 15, 2022

Published: March 7, 2022

## REFERENCES

- Ellmer, K. (2012). Past achievements and future challenges in the development of optically transparent electrodes. *Nat. Photonics* 6, 809–817.
- Yu, X., Marks, T.J., and Faccetti, A. (2016). Metal oxides for optoelectronic applications. *Nat. Mater.* 15, 383–396.
- Morales-Masis, M., De Wolf, S., Woods-Robinson, R., Ager, J.W., and Ballif, C. (2017). Transparent electrodes for efficient optoelectronics. *Adv. Electron. Mater.* 3, 1600529.
- Shi, J., Zhang, J., Yang, L., Qu, M., Qi, D.C., and Zhang, K.H.L. (2021). Wide bandgap oxide semiconductors: from materials physics to optoelectronic devices. *Adv. Mater.* 33, e2006230.
- Kneissl, M., Seong, T.-Y., Han, J., and Amano, H. (2019). The emergence and prospects of deep-ultraviolet light-emitting diode technologies. *Nat. Photonics* 13, 233–244.
- Park, Y., Roth, J., Oka, D., Hirose, Y., Hasegawa, T., Paul, A., Pogrebnyakov, A., Gopalan, V., Birol, T., and Engel-Herbert, R. (2020). SrNbO<sub>3</sub> as a transparent conductor in the visible and ultraviolet spectra. *Commun. Phys.* 3, 102.
- Kim, H.-D., An, H.-M., Kim, K.H., Kim, S.J., Kim, C.S., Cho, J., Schubert, E.F., and Kim, T.G. (2014). A universal method of producing transparent electrodes using wide-bandgap materials. *Adv. Funct. Mater.* 24, 1575–1581.
- Hosono, H. (2007). Recent progress in transparent oxide semiconductors: materials and device application. *Thin Solid Films* 515, 6000–6014.
- Zaumseil, J., and Sirringhaus, H. (2007). Electron and ambipolar transport in organic field-effect transistors. *Chem. Rev.* 107, 1296–1323.
- Gwinner, M.C., Vaynzof, Y., Banger, K.K., Ho, P.K.H., Friend, R.H., and Sirringhaus, H. (2010). Solution-processed zinc oxide as high-performance air-stable electron injector in organic ambipolar light-emitting field-effect transistors. *Adv. Funct. Mater.* 20, 3457–3465.
- Zhou, Y., Fuentes-Hernandez, C., Shim, J., Meyer, J., Giordano, A.J., Li, H., Winget, P., Papadopoulos, T., Cheun, H., Kim, J., et al. (2012). A universal method to produce low-work function electrodes for organic electronics. *Science* 336, 327–332.
- Hosono, H., Kim, J., Toda, Y., Kamiya, T., and Watanabe, S. (2017). Transparent amorphous oxide semiconductors for organic electronics: application to inverted OLEDs. *Proc. Natl. Acad. Sci. U S A* 114, 233–238.
- Matsuishi, S., Toda, Y., Miyakawa, M., Hayashi, K., Kamiya, T., Hirano, M., Tanaka, I., and Hosono, H. (2003). High-density electron anions in a nanoporous single crystal: [Ca<sub>24</sub>Al<sub>28</sub>O<sub>64</sub>]<sup>4+</sup>(4e<sup>-</sup>). *Science* 301, 626–629.
- Miyakawa, M., Hirano, M., Kamiya, T., and Hosono, H. (2007). High electron doping to a wide band gap semiconductor 12CaO·7Al<sub>2</sub>O<sub>3</sub> thin film. *Appl. Phys. Lett.* 90, 182105.
- Zhang, D., Zheng, W., Zheng, Q., Chen, A., Ji, X., and Huang, F. (2016). A strategy of transparent conductive oxide for UV focal plane array detector: two-step thermodynamic process. *Adv. Electron. Mater.* 2, 1600320.
- Wei, M., Sanchela, A.V., Feng, B., Ikuhara, Y., Cho, H.J., and Ohta, H. (2020). High electrical conducting deep-ultraviolet-transparent oxide semiconductor La-doped SrSnO<sub>3</sub> exceeding ~3000 S cm<sup>-1</sup>. *Appl. Phys. Lett.* 116, 022103.
- Pearson, S.J., Yang, J., Cary, P.H., Ren, F., Kim, J., Tadjer, M.J., and Mastro, M.A. (2018). A review of Ga<sub>2</sub>O<sub>3</sub> materials, processing, and devices. *Appl. Phys. Rev.* 5, 011301.
- Chen, X., Ren, F., Gu, S., and Ye, J. (2019). Review of gallium-oxide-based solar-blind ultraviolet photodetectors. *Photonics Res.* 7, 381–415.
- Zhang, J., Shi, J., Qi, D.-C., Chen, L., and Zhang, K.H.L. (2020). Recent progress on the electronic structure, defect, and doping properties of Ga<sub>2</sub>O<sub>3</sub>. *APL Mater.* 8, 020906.
- Villora, E.G., Shimamura, K., Yoshikawa, Y., Ujiie, T., and Aoki, K. (2008). Electrical conductivity and carrier concentration control in β-Ga<sub>2</sub>O<sub>3</sub> by Si doping. *Appl. Phys. Lett.* 92, 202120.
- Zhang, F., Arita, M., Wang, X., Chen, Z., Saito, K., Tanaka, T., Nishio, M., Motooka, T., and Guo, Q. (2016). Toward controlling the carrier density of Si doped Ga<sub>2</sub>O<sub>3</sub> films by pulsed laser deposition. *Appl. Phys. Lett.* 109, 102105.
- Leedy, K.D., Chabak, K.D., Vasilyev, V., Look, D.C., Boeckl, J.J., Brown, J.L., Tetlak, S.E., Green, A.J., Moser, N.A., Crespo, A., et al. (2017). Highly conductive homoepitaxial Si-doped Ga<sub>2</sub>O<sub>3</sub> films on (010) β-Ga<sub>2</sub>O<sub>3</sub> by pulsed laser deposition. *Appl. Phys. Lett.* 111, 012103.
- Ahmadi, E., Koksaldi, O.S., Kaun, S.W., Oshima, Y., Short, D.B., Mishra, U.K., and Speck, J.S. (2017). Ge doping of β-Ga<sub>2</sub>O<sub>3</sub> films grown by plasma-assisted molecular beam epitaxy. *Appl. Phys. Express* 10, 041102.
- Orita, M., Ohta, H., Hirano, M., and Hosono, H. (2000). Deep-ultraviolet transparent conductive β-Ga<sub>2</sub>O<sub>3</sub> thin films. *Appl. Phys. Lett.* 77, 4166–4168.
- Zhang, Y., Joishi, C., Xia, Z., Brenner, M., Lodha, S., and Rajan, S. (2018). Demonstration of β-(Al<sub>x</sub>Ga<sub>1-x</sub>)<sub>2</sub>O<sub>3</sub>/Ga<sub>2</sub>O<sub>3</sub> double heterostructure field effect transistors. *Appl. Phys. Lett.* 112, 233503.
- Roy, R., Hill, V.G., and Osborn, E.F. (1952). Polymorphism of Ga<sub>2</sub>O<sub>3</sub> and the system Ga<sub>2</sub>O<sub>3</sub>-H<sub>2</sub>O. *J. Am. Chem. Soc.* 74, 719–722.
- He, H., Orlando, R., Blanco, M.A., Pandey, R., Amzallag, E., Baraille, I., and Rérat, M. (2006). First-principles study of the structural, electronic, and optical properties of Ga<sub>2</sub>O<sub>3</sub> in

- its monoclinic and hexagonal phases. *Phys. Rev. B* 74, 195123.
28. Varley, J.B., Weber, J.R., Janotti, A., and Van de Walle, C.G. (2010). Oxygen vacancies and donor impurities in  $\beta$ -Ga<sub>2</sub>O<sub>3</sub>. *Appl. Phys. Lett.* 97, 142106.
  29. Lany, S. (2018). Defect phase diagram for doping of Ga<sub>2</sub>O<sub>3</sub>. *APL Mater.* 6, 046103.
  30. Passlack, M., Hunt, N.E.J., Schubert, E.F., Zydzik, G.J., Hong, M., Mannaerts, J.P., Opila, R.L., and Fischer, R.J. (1994). Dielectric properties of electron-beam deposited Ga<sub>2</sub>O<sub>3</sub> films. *Appl. Phys. Lett.* 64, 2715–2717.
  31. Mohamed, M., Janowitz, C., Unger, I., Manzke, R., Galazka, Z., Uecker, R., Fornari, R., Weber, J.R., Varley, J.B., and Van de Walle, C.G. (2010). The electronic structure of  $\beta$ -Ga<sub>2</sub>O<sub>3</sub>. *Appl. Phys. Lett.* 97, 211903.
  32. Mott, N.F. (1961). The transition to the metallic state. *Philos. Mag.* 6, 287–309.
  33. Leedy, K.D., Chabak, K.D., Vasilyev, V., Look, D.C., Mahalingam, K., Brown, J.L., Green, A.J., Bowers, C.T., Crespo, A., Thomson, D.B., and Jessen, G.H. (2018). Si content variation and influence of deposition atmosphere in homoepitaxial Si-doped  $\beta$ -Ga<sub>2</sub>O<sub>3</sub> films by pulsed laser deposition. *APL Mater.* 6, 101102.
  34. Baldini, M., Albrecht, M., Fiedler, A., Irmscher, K., Schewski, R., and Wagner, G. (2016). Si- and Sn-doped homoepitaxial  $\beta$ -Ga<sub>2</sub>O<sub>3</sub> layers grown by MOVPE on (010)-oriented substrates. *ECS J. Solid State Sci. Technol.* 6, Q3040–Q3044.
  35. Nakagomi, S., and Kokubun, Y. (2012). Crystal orientation of  $\beta$ -Ga<sub>2</sub>O<sub>3</sub> thin films formed on c-plane and a-plane sapphire substrate. *J. Cryst. Growth* 349, 12–18.
  36. Nakagomi, S., and Kokubun, Y. (2013). Cross-sectional TEM imaging of  $\beta$ -Ga<sub>2</sub>O<sub>3</sub> thin films formed on c-plane and a-plane sapphire substrates. *Phys. Status Solidi A* 210, 1738–1744.
  37. Burstein, E. (1954). Anomalous optical absorption limit in InSb. *Phys. Rev.* 93, 632–633.
  38. Moss, T.S. (1954). The interpretation of the properties of indium antimonide. *Proc. Phys. Soc. B* 67, 775–782.
  39. Haacke, G. (1976). New figure of merit for transparent conductors. *J. Appl. Phys.* 47, 4086–4089.
  40. Bisht, H., Eun, H.T., Mehrtens, A., and Aegeerter, M.A. (1999). Comparison of spray pyrolyzed FTO, ATO and ITO coatings for flat and bent glass substrates. *Thin Solid Films* 351, 109–114.
  41. Ellmer, K., and Mientus, R. (2008). Carrier transport in polycrystalline ITO and ZnO:Al II: the influence of grain barriers and boundaries. *Thin Solid Films* 516, 5829–5835.
  42. Reese, S.B., Remo, T., Green, J., and Zakutayev, A. (2019). How much will gallium oxide power electronics cost? *Joule* 3, 903–907.
  43. Scofield, J.H. (1973). Theoretical photoionization cross sections from 1 to 1500 keV. In Technical Report UCRL-51326 (Lawrence Livermore Laboratory).
  44. Berggren, K.F., and Sernelius, B.E. (1981). Band-gap narrowing in heavily doped many-valley semiconductors. *Phys. Rev. B* 24, 1971–1986.
  45. Jou, J.-H., Kumar, S., Agrawal, A., Li, T.-H., and Sahoo, S. (2015). Approaches for fabricating high efficiency organic light emitting diodes. *J. Mater. Chem. C* 3, 2974–3002.
  46. Scanlon, D.O., and Watson, G.W. (2012). On the possibility of p-type SnO<sub>2</sub>. *J. Mater. Chem.* 22, 25236.
  47. Höffling, B., Schleife, A., Rödl, C., and Bechstedt, F. (2012). Band discontinuities at Si-TCO interfaces from quasiparticle calculations: comparison of two alignment approaches. *Phys. Rev. B* 85, 035305.
  48. Walsh, A., Buckeridge, J., Catlow, C.R.A., Jackson, A.J., Keal, T.W., Miskufova, M., Sherwood, P., Shevlin, S.A., Watkins, M.B., Woodley, S.M., and Sokol, A.A. (2013). Limits to doping of wide band gap semiconductors. *Chem. Mater.* 25, 2924–2926.
  49. Wei, S.-H., and Zunger, A. (1999). Predicted band-gap pressure coefficients of all diamond and zinc-blende semiconductors: chemical trends. *Phys. Rev. B* 60, 5404–5411.
  50. Zhang, S.B., Wei, S.-H., and Zunger, A. (1998). A phenomenological model for systematization and prediction of doping limits in II-VI and I-III-VI<sub>2</sub> compounds. *J. Appl. Phys.* 83, 3192–3196.
  51. Zhang, S.B. (2002). The microscopic origin of the doping limits in semiconductors and wide-gap materials and recent developments in overcoming these limits: a review. *J. Phys. Condens. Matter* 14, R881–R903.
  52. Scanlon, D.O., Regoutz, A., Egdell, R.G., Morgan, D.J., and Watson, G.W. (2013). Band gap engineering of In<sub>2</sub>O<sub>3</sub> by alloying with Ti<sub>2</sub>O<sub>3</sub>. *Appl. Phys. Lett.* 103, 262108.
  53. Sobola, D., Tălu, Š., Solaymani, S., and Grmela, L. (2017). Influence of scanning rate on quality of AFM image: study of surface statistical metrics. *Microsc. Res. Tech.* 80, 1328–1336.
  54. Tălu, Š. (2015). Micro and nanoscale characterization of three dimensional surfaces. In Basics and Applications (Napoca Star Publishing house).
  55. Yeh, J.J., and Lindau, I. (1985). Atomic subshell photoionization cross sections and asymmetry parameters:  $1 \leq Z \leq 103$ . *Atom. Data Nucl. Data Tables* 32, 1–155.
  56. Kresse, G., and Furthmüller, J. (1996). Efficient iterative schemes for ab initio total-energy calculations using a plane-wave basis set. *Phys. Rev. B* 54, 11169–11186.
  57. Kresse, G., and Furthmüller, J. (1996). Efficiency of ab-initio total energy calculations for metals and semiconductors using a plane-wave basis set. *Comput. Mater. Sci.* 6, 15–50.
  58. Kresse, G., and Hafner, J. (1994). Ab initio molecular-dynamics simulation of the liquid-metal–amorphous-semiconductor transition in germanium. *Phys. Rev. B* 49, 14251–14269.
  59. Kresse, G., and Hafner, J. (1993). Ab initio molecular dynamics for liquid metals. *Phys. Rev. B* 47, 558–561.
  60. Blöchl, P.E. (1994). Projector augmented-wave method. *Phys. Rev. B* 50, 17953–17979.
  61. Kresse, G., and Joubert, D. (1999). From ultrasoft pseudopotentials to the projector augmented-wave method. *Phys. Rev. B* 59, 1758–1775.
  62. Krukau, A.V., Vydrov, O.A., Izmaylov, A.F., and Scuseria, G.E. (2006). Influence of the exchange screening parameter on the performance of screened hybrid functionals. *J. Chem. Phys.* 125, 224106.
  63. Peelaers, H., and Van de Walle, C.G. (2015). Brillouin zone and band structure of  $\beta$ -Ga<sub>2</sub>O<sub>3</sub>. *Phys. Status Solidi B* 252, 828–832.
  64. Deák, P., Duy Ho, Q., Seemann, F., Aradi, B., Lörke, M., and Frauenheim, T. (2017). Choosing the correct hybrid for defect calculations: a case study on intrinsic carrier trapping in  $\beta$ -Ga<sub>2</sub>O<sub>3</sub>. *Phys. Rev. B* 95, 075208.
  65. Broberg, D., Medasani, B., Zimmermann, N.E.R., Yu, G., Canning, A., Haranczyk, M., Asta, M., and Hautier, G. (2018). PyCDT: a Python toolkit for modeling point defects in semiconductors and insulators. *Comput. Phys. Commun.* 226, 165–179.
  66. Ganose, A.M., Jackson, A.J., and Scanlon, D.O. (2018). sumo: command-line tools for plotting and analysis of periodic ab initio calculations. *J. Open Source Softw.* 3, 717.